Chapter 6

Band Gap Engineering Through Calcium Addition in (Mg,Co,Ni,Cu,Zn)O High Entropy Oxide for Efficient Photocatalysis

6.1 Introduction

High entropy oxides (HEOs) have garnered significant attention in recent years due to their remarkable compositional versatility, chemical and thermal stability, and unique redox behaviour, making them promising for various functional applications. Inspired by the concept of high entropy alloys (HEAs) [10,11], the stabilization of multicomponent HEOs relies on the balance between the enthalpy of mixing (ΔH_{mix}) and a substantial positive configurational entropy (ΔS_{mix}), which minimizes the Gibbs free energy ($\Delta G_{mix} = \Delta H_{mix} - T\Delta S_{mix}$) and enables the formation of stable single phase solid solutions [22,45]. The discovery of entropy-stabilized HEOs, with cations like Mg^{2+}, Ni^{2+}, Zn^{2+}, Cu^{2+} and Co^{2+} randomly distributed in a rocksalt lattice, has catalyzed research into their diverse applications, such as photocatalysis [6,169–171,173], electrocatalysis [237–239], and energy storage [62,155,174]. In particular, the photocatalytic potential of HEOs is of great interest due to their multi-electron redox properties [28,166,240], lattice distortion-induced oxygen defects [49,98,146,148], and exceptional thermal stability [73,153,166], which provide significant advantages over traditional catalysts, including TiO_2 and ZnO [167,194,241–244]. The catalytic advantage of high entropy oxides (HEOs) lies in the synergy between their multicomponent

lattice confinement and oxygen defects induced by lattice distortion [245]. This unique combination enhances their activity and stability, making HEOs a promising candidate for addressing critical environmental challenges, such as dye pollution in aquatic ecosystems. Dye pollutants are a major ecological hazard. Photocatalysis has emerged as an effective and sustainable technology for degrading the dye pollutants. Photocatalytic reactions are initiated when photons with energy equal to or greater than the catalyst's band gap energy (E_g) are absorbed, generating electron-hole pairs on the catalyst surface. These reactive species subsequently degrade organic pollutants into environmentally benign products like CO_2 and H_2O, eliminating the need for complex separation processes. Among conventional photocatalysts, TiO_2 and ZnO are widely used for dye degradation. However, their wide band gaps restrict photoactivity to the UV range, which constitutes only 5% of the solar spectrum, significantly limiting their efficiency under solar illumination. This limitation has driven research into advanced photocatalysts like HEOs, which offer enhanced redox properties, tunable band gaps, and the potential for visible-light activation, providing a sustainable solution for wastewater treatment. Despite extensive research, the photocatalytic efficiency of TiO_2 and ZnO in the visible light spectrum remains limited, even with metal or nonmetal doping. These modifications face technical challenges, hindering their full potential for effective visible-light utilization [26,166]. On the other hand, noble metals like platinum and rhodium are widely recognized for their exceptional catalytic properties. Their unfilled d orbitals allow for the formation of coordination bonds, making them highly effective participants in catalytic reactions [246]. Additionally, their surfaces resist the adsorption of reactants and byproducts, ensuring continuous

availability of active sites. Noble metals also boast superior oxidation and corrosion resistance, further enhancing their suitability for catalytic applications [169,247]. However, the natural scarcity and high cost of noble metals pose significant barriers to their widespread use. These challenges drive the exploration of alternative catalysts, such as high entropy oxides, that offer comparable performance while addressing the economic and sustainability concerns associated with noble metals [168,205]. Doping high-entropy oxides (HEOs) with larger cations compared to the parent cations introduce significant lattice defects due to ionic radius mismatch, which can substantially enhance photocatalytic activity. Calcium (Ca^{2+}) emerges as an ideal dopant, with its larger ionic radius (0.99 Å) compared to the average ionic radius (0.72 Å) of the host cations in the parent five-component oxide (Mg,Co,Ni,Cu,Zn)O. The incorporation of Ca^{2+} induces lattice strain, which is alleviated by the formation of defects such as metal or oxygen vacancies [214,243]. These defects serve as active sites, boosting the photocatalytic performance. Furthermore, as the least electronegative cation in the HEO, Ca^{2+} promotes the generation of electron-hole pairs (e^- and h^+). When these charged species interact with water molecules in an aqueous medium, they generate highly reactive •OH radicals, which play a pivotal role in the efficient degradation of organic dyes [248,249]. This dual role of Ca^{2+} in inducing lattice defects and enhancing redox activity makes it a powerful modifier for improving the photocatalytic capabilities of HEOs.

In this chapter, we have discussed the calcium-incorporated single-phase rocksalt high-entropy oxides (HEOs) of the composition $(Mg,Co,Ni,Cu,Zn)_{1-x}Ca_xO$,

synthesized via the solution combustion synthesis (SCS) route with varying Ca^{2+} concentrations (x = 0.05, 0.1). The photocatalytic performance of these synthesized HEOs was evaluated for methylene blue (MB) degradation under solar illumination. The investigation highlights the critical role of Ca^{2+} doping in altering the structural and optical properties of (Mg,Co,Ni,Cu,Zn)O, resulting in enhanced visible light photocatalytic activity. For the simplicity (Mg,Co,Ni,Cu,Zn)O, $(Mg,Co,Ni,Cu,Zn)_{0.95}Ca_{0.05}O$, $(Mg,Co,Ni,Cu,Zn)_{0.90}Ca_{0.10}O$ will be denoted as TM-HEO0, TM-HEO5, and TM-HEO10, respectively.

6.2 Experimental details

6.2.1 Materials and catalyst preparation

Metal nitrates were utilized to synthesize nanocrystalline $(Mg,Co,Ni,Cu,Zn)_{1-x}Ca_x$ O (x=0, 0.05, 0.1) powder by (SCS) technique as discussed in Chapter 3. For uniformity in processing, calcination was carried out at 1373 K for 2 h and followed by quenching in air, which resulted in high entropy oxide powder catalysts (Mg,Co,Ni,Cu,Zn)O, and $(Mg,Co,Ni,Cu,Zn)_{1-x}Ca_xO$ (x = 0.05, 0.1). Here onwards, (Mg,Co,Ni,Cu,Zn)O, $(Mg,Co,Ni,Cu,Zn)_{0.95}Ca_{0.05}O$, $(Mg,Co,Ni,Cu,Zn)_{0.90}Ca_{0.10}O$ will be denoted as TM-HEO0, TM-HEO5, and TM-HEO10, respectively.

6.2.2 Characterization

XRD patterns were recorded in the 2θ range of 20° to 80° with a step size of 0.02 and at a scan rate of 2°/ min. Transmission electron microscopy images and selected area diffraction pattern (SAED) were recorded by TEM (Tecnai G2 20 TWIN, FEI) under an operating voltage of 200 kV. Samples for TEM imaging were prepared by dispersing the powder in ethanol through ultrasonication for 60 min followed by

drop-casting on a 200-mesh carbon-coated Cu grid. Surface area measurements were performed by nitrogen adsorption at 77 K (BET, Bellsorp Max ii & Belcat-ii) using the Brunauer-Emmett-Teller (BET) method. The UV-vis absorption and FT-IR spectra were studied using a UV-vis spectrometer (Perkin -Elmer lambda 800) and Nicolet iS5 FT-IR Spectrometer, respectively. X-ray photoelectron spectroscopy was performed in Thermo Fisher Scientific (K-Alpha) XPS system using Al-K_α at 1486 eV as an X-ray probe. All the binding energies of XPS spectra were calibrated to C1s at 284.8eV. UV-vis absorption spectra of MB dye solution were recorded on a UV-vis (V-770 Spectrophotometer, JASCO Inc.) spectrometer with a step size of 1nm.

6.2.3 Photocatalytic activity measurement

Photocatalytic activities of catalysts were analyzed by monitoring the degradation of methylene blue (MB) dye at room temperature (27°C) under visible light. Batch experiments were performed in a petri dish containing 50 mL of 10 ppm MB dye mixed with 60 mg of HEO catalyst synthesized by the SCS technique. The aqueous dye solution with catalyst was continuously stirred using a magnetic stirrer for 60 min in dark conditions to obtain the adsorption-desorption state of equilibrium. Subsequently, the mixture was exposed to visible light for a total duration of 80 min using a 100 mW/cm^2 solar simulator. During the irradiation, 3 ml of solution was drawn every 20 min using a syringe, and catalysts were separated using a Whatman® filter paper to study the photodegradation of dye with time.

6.3 Results and discussion:

6.3.1 XRD and morphological characteristics

X-ray diffraction (XRD) was employed to analyze the phase and structural parameters of the synthesized TM-HEO0 (**Figure 6.1a**), TM-HEO5 (**Figure 6.1b**), and TM-HEO10 powders (**Figure 6.1c**). The diffraction patterns confirmed that all samples exhibited a single-phase rocksalt structure (space group $Fm\bar{3}m$), with no secondary phases detected. The XRD patterns of TM-HEO5 and TM-HEO10 were nearly identical to those of TM-HEO0, suggesting successful incorporation of Ca^{2+} ions into the rocksalt lattice without the formation of additional phases. Despite this, the larger ionic radius of Ca^{2+} (0.99 Å) compared to the average size of the host cations (0.7 Å) introduces lattice strain, which can impose a solubility limit [33]. Interestingly, such size-induced strain effects are sometimes mitigated in nanoscale crystals, allowing for higher solubility than expected [250]. A subtle shift of the (200) peak towards lower 2θ values (**Figure 6.1d**) with increasing Ca^{2+} concentration was observed, indicative of an expansion in the lattice parameter [214,251–253].

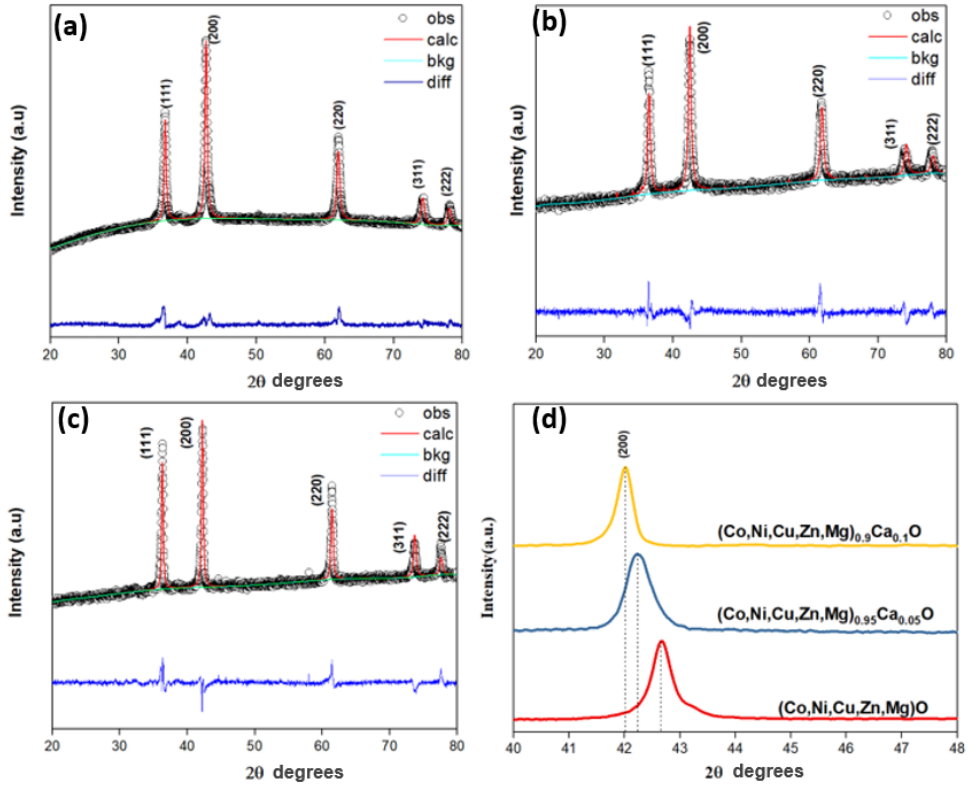

Figure 6.1 Rietveld refined XRD pattern of (a) TM-HEO0 (b) TM-HEO5 (c) TM-HEO10 showing single phase rocksalt phase. (d) left shift of high-intensity peak (200) indicates lattice expansion.

The photocatalytic activity of HEOs is largely influenced by their surface area and active site density, which are governed by factors such as morphology, crystallite size, and the uniform distribution of elements. **Figure 6.2(a-d)** illustrates TEM images of TM-HEO0 and TM-HEO10, providing insights into their morphology. The insets show the corresponding selected area electron diffraction (SAED) patterns, featuring well-defined intense rings corresponding to the (111), (200), (220), (311), (222), and (400) planes, consistent with the XRD data. These results confirm a well-crystallized rocksalt structure with no detectable secondary phases. TEM images reveal agglomerated particles with a predominantly equiaxed

morphology. Notably, the particle sizes in the TM-HEO10 samples were smaller compared to TM-HEO0. Additionally, the lattice fringes observed with interplanar spacings of 0.243 nm and 0.247 nm for TM-HEO0 and TM-HEO10, respectively, correspond to the (111) crystal planes, further confirming the high crystallinity of the synthesized materials.

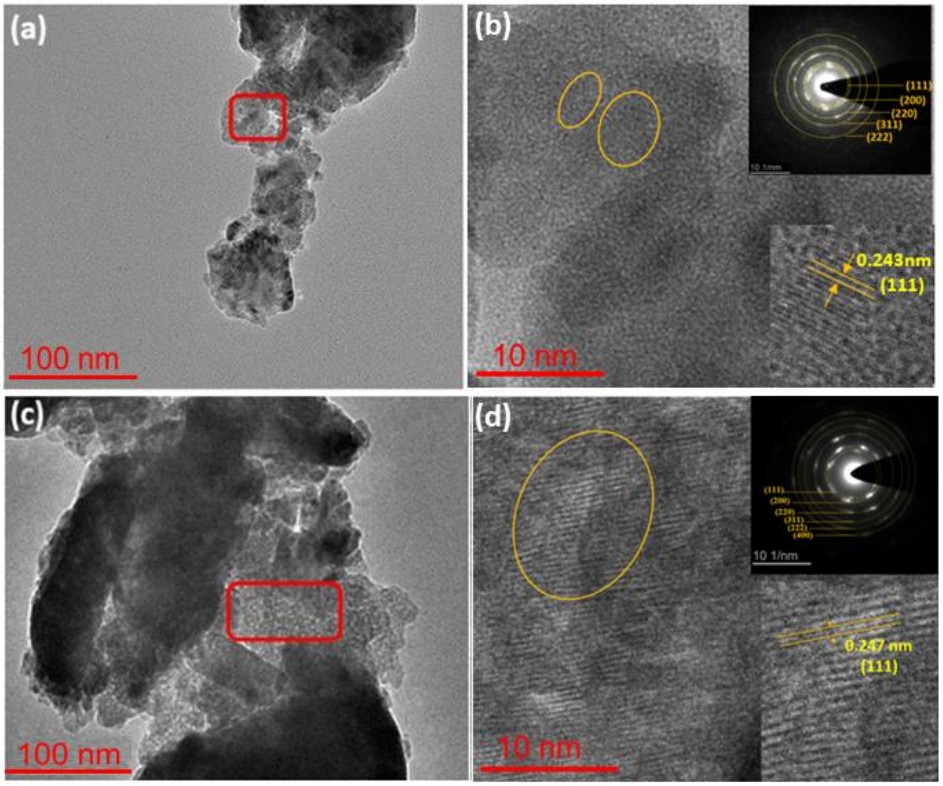

Figure 6.2 TEM images of (a-b) TM-HEO0 and corresponding SAED pattern (inset) (c-d) TM-HEO10 and corresponding SAED pattern (inset).

6.3.2 FTIR analysis

The FTIR spectra of the synthesized samples (**Figure 6.3a**) reveal multiple absorption bands corresponding to characteristic functional groups. The broad absorption peaks at 3440 cm^{-1} and 1630 cm^{-1} are attributed to O-H stretching and bending vibrational modes on the catalyst surface, respectively [254,255], while the band at 1480 cm^{-1} corresponds to C-H bending vibrations [41]. Notably, the addition of Ca^{2+} resulted in an increased intensity of the 3440 cm^{-2} band and the emergence of a sharp peak at 3647 cm^{-2}, indicative of an additional O-H band [199]. This enhancement in hydroxyl group abundance is likely due to the creation of vacancies, which was further corroborated by XPS analysis. These vacancies serve as active sites, enhancing photocatalytic performance.

6.3.3 BET analysis

Figure 6.3(b) presents the N_2 adsorption-desorption isotherms of the synthesized nanocrystalline powders TM-HEO0, TM-HEO5, and TM-HEO10. The isotherms exhibit a type IV pattern, characteristic of mesoporous materials, with adsorption-desorption hysteresis in the P/P_0 range of 0.57-0.99. This hysteresis corresponds to a type H_2 loop, indicative of the mesoporous nature of the powders [245]. The multi-point BET surface area measurements revealed that TM-HEO10 and TM-HEO5 exhibit surface areas of 41 m^2/g and 29 m^2/g, respectively, with average pore diameters of 11.2 nm and 15.8 nm. In contrast, TM-HEO0 showed a lower surface area of 13 m^2/g and a larger average pore diameter of 18.7 nm. The higher surface area observed in TM-HEO10 and TM- HEO5 is expected to enhance photocatalytic efficiency by providing an increased number of active sites.

6.3.4 UV-vis spectroscopy

UV-vis spectroscopy was employed to investigate the optical absorption and band gap properties of the synthesized powders. The absorption spectra of TM-HEO0, TM-HEO5, and TM-HEO10 (**Figure 6.3c** and **6.3d**) reveal that the incorporation of Ca^{2+} significantly enhances the light absorption capability of the multicomponent oxide system in the visible region. Additionally, the absorption edge undergoes a redshift, indicating a decrease in the band gap with the incorporation of Ca^{2+} into TM-HEOs. The optical band gap, E_g, was estimated from UV spectra using Tauc plot ($(\alpha h\nu)^2$ vs. $h\nu$). The linear region of the curve was extrapolated to the energy axis according to the relation given in equation 2 [256,257].

$$(\alpha h\nu)^2 = A\,(h\nu - E_g) \qquad (1)$$

where '*hν'* is the photon energy, 'α' is absorbance, and 'A' is the proportionality constant. The estimated optical band gap of TM-HEO0, TM-HEO5 and TM-HEO10 samples are 1.33, 1.25 and 1.18 eV, respectively. Although the individual constituent oxides of TM-HEO0 typically have wide band gaps, the band gap of TM-HEO0 is surprisingly narrow at only 1.33 eV. This unexpected result can be attributed to the shifting of d-band energy levels. Each constituent oxide in TM-HEO0 exhibits distinct electronegativity (χ) and crystal field splitting (Δ), which introduces multiple 3d states within the native band gap. This interaction effectively narrows the overall band gap [258], contributing to the enhanced optical properties of the material. When a large cation like Ca^{2+} (ionic radius ~0.99 Å) is incorporated into the host lattice (with an average ionic radius~0.7 Å), strain is induced.

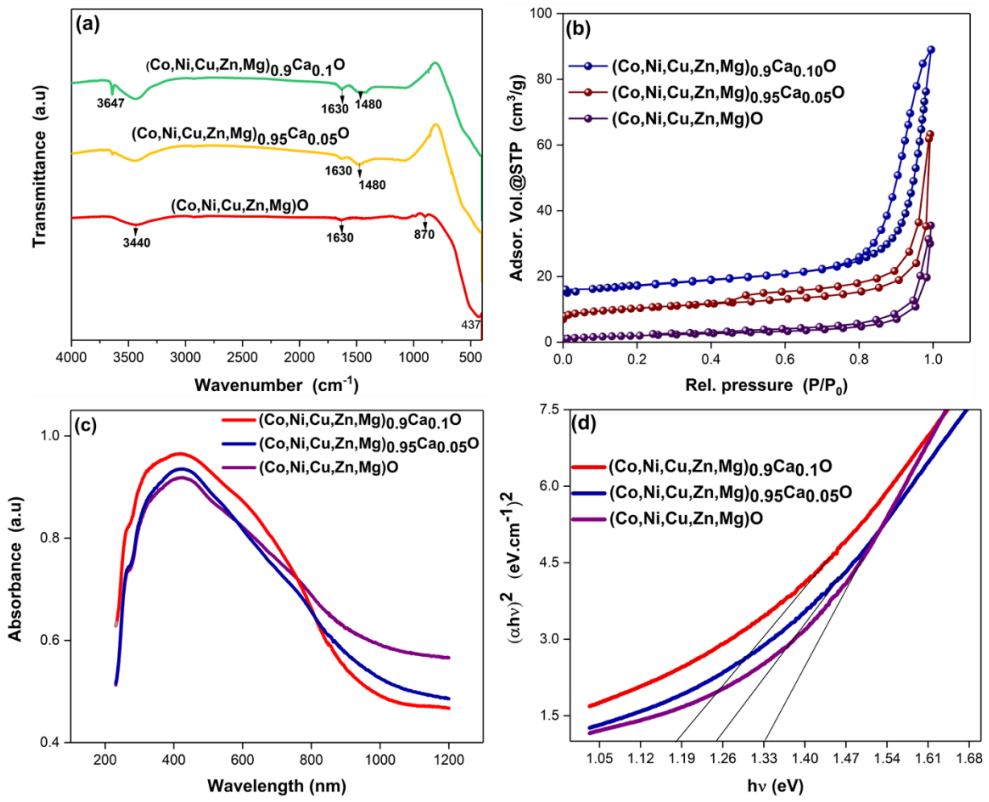

Figure 6.3 (a) FT-IR spectra of all synthesized nanocrystalline powder, (b) N_2 absorption -desorption isotherm curves, (c) UV-vis absorption spectra and (d) Tauc plot of all the samples (TM-HEO0, TM-HEO5 and TM-HEO10).

To alleviate this strain, Ni^{2+} and Co^{2+} ions tend to reduce their ionic radii and adopt a +3 oxidation state, thereby increasing the covalency factor, as observed in the XPS spectra. This enhanced covalency strengthens the hybridization between the O *2p* and transition metal (TM) 3d orbitals, which in turn lowers the charge transfer energy. Additionally, for charge compensation, a fraction of Cu^{2+} ions shifts to the +1 oxidation state, reducing the crystal field splitting (Δ) and subsequently narrowing the band gap [114]. Furthermore, the introduction of the lower energy Ca^{2+} *3s* state, compared to the TM *4s* state in the conduction band [258,259], further contributes to the reduction in the band gap, as previously reported. A lower band

gap improves the absorbance in the visible region, promoting photocatalytic activity as a broader region of the solar spectrum can be utilized [260].

6.3.5 Photocatalytic activity and rate kinetics

The photocatalytic performance of TM-HEO catalysts was evaluated by irradiating a 10 ppm aqueous MB dye solution with a 100 mW/cm^2 solar simulator at room temperature (27°C). Using 60 mg of catalyst under visible light exposure, the degradation of MB dye was monitored through the absorption peak at 664 nm (**Figure 6.4**), which showed a marked decrease over time. The results revealed significant dye degradation rates of 40%, 78%, and 97% within 80 minutes for TM-HEO0, TM-HEO5, and TM-HEO10, respectively, as determined using the Beer-Lambert law. This highlights the superior catalytic efficiency of TM-HEO10. The MB degradation was also performed without the catalyst under illumination and with the catalyst in the dark to demonstrate the effectiveness of the catalyst. Only a negligible degradation (<7%) of MB dye happened in 80 min in both conditions as shown in **Figure 6.5**. This confirms the role of the photocatalyst in degrading the MB dye. The normalized dye concentration (C/C_0) is plotted against time (**Figure 6.6**). The linear nature of the ln (C_0/C) vs. time plot shows that the degradation follows a first-order kinetics as shown in **Figure 6.7a**. The photocatalytic degradation with respect to time is fitted using the modified rate expression for first-order kinetics (as per equation 2) [255,261]:

$$\ln\left(\frac{C_0}{C}\right) = kt \qquad (2)$$

where '*k*' is the rate constant of the degradation reaction and '*t*' is the irradiation time. The rate constant estimated by linear fit was about 0.0071, 0.0144, and 0.0445 min^{-1} for TM-HEO0, TM-HEO5, and TM-HEO10 catalysts, respectively. Catalytic activity can also increase due to the increase in specific surface area.

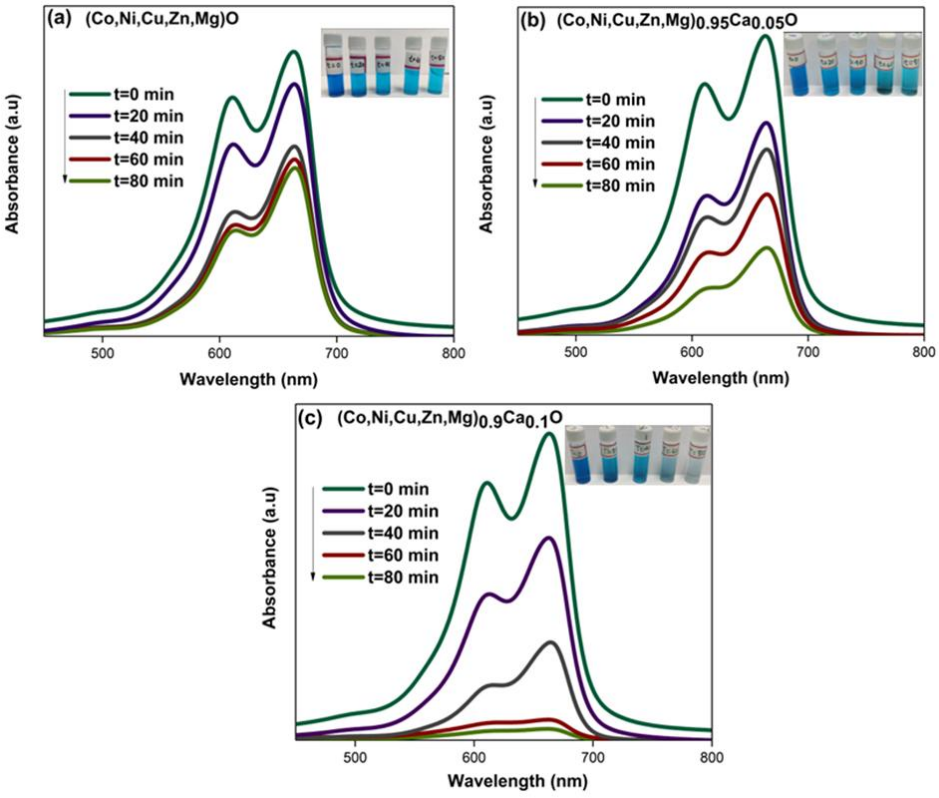

Figure 6.4 UV-vis spectra of MB degradation when exposed to the visible light source (100 $mWcm^{-2}$ solar simulator) at 80 min irradiation time in the presence of photocatalyst (a) TM-HEO0 (b) TM-HEO5 (c) TM-HEO10.

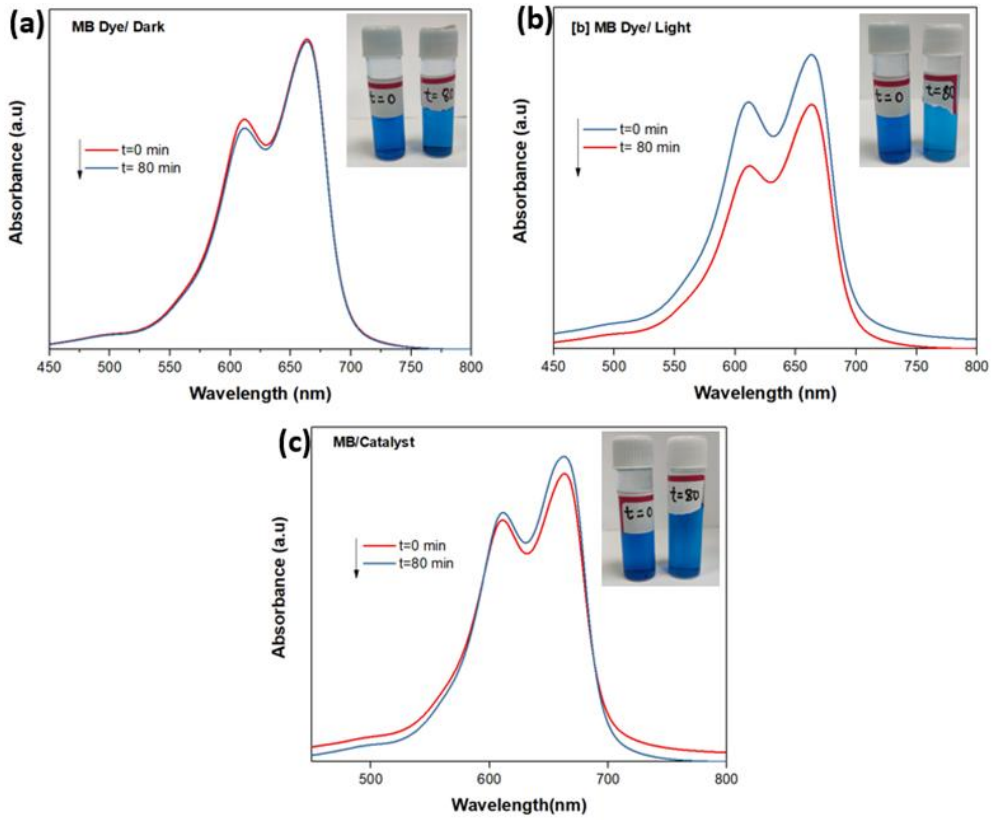

Figure 6.5 The absorbance spectra of MB Solution without catalyst under (a) dark (b) light condition (c) with Catalyst under dark condition.

However, in this case, the increase in specific surface area was hardly three times; however, the rate increased by more than 6 times. Further, the increase in surface area could also be ascribed to the Ca^{2+} addition, which increased lattice strain and restricted the grain growth during processing. This clearly shows that the incorporation of 10% Ca^{2+} cations in TM-HEO0, enhances the photocatalytic activity by up to six times (**Figure 6.7b**). The photodegradation achieved in this work using TM-HEO10 catalyst exceeds any other reported multicomponent HEO catalyst. A comparison of the reported degradation achieved using multicomponent TM oxide catalysis with the TM-HEO10 is given in **Table 6.1**.

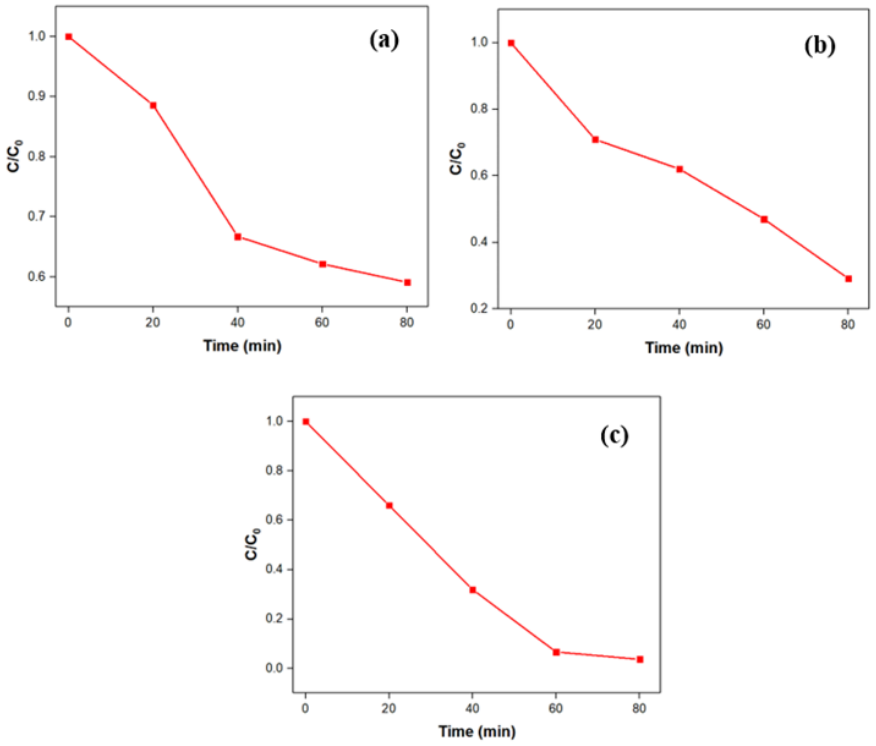

Figure 6.6 Relative concentration (C/C_0) with irradiation time for (a)TM-HEO0 (b) TM-HEO5 (c) TM-HEO10.

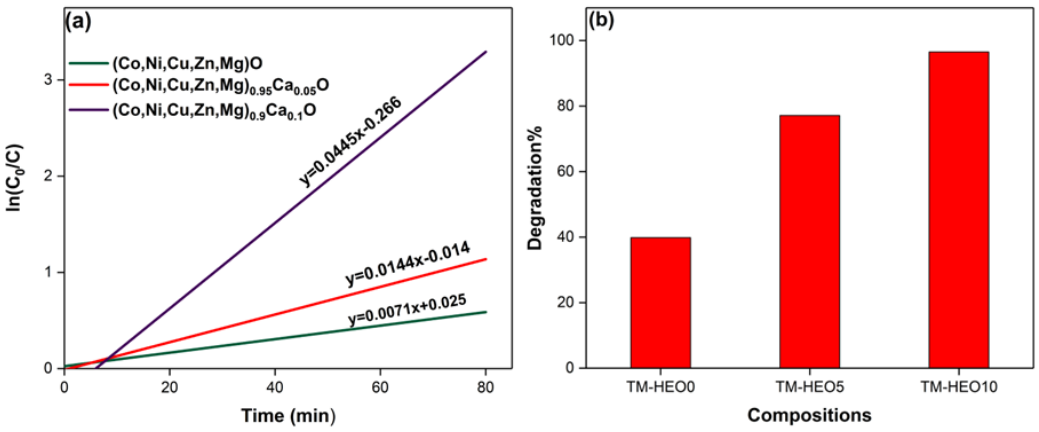

Figure 6.7 (a) The comparative rate kinetics plots of photocatalytic dye degradation redox reaction and (b) the corresponding dye degradation percentage.

6.3.6 XPS analysis

X-ray photoelectron spectroscopy (XPS) was conducted to get insight into the oxidation states of transition metal cations in the catalyst. The high-resolution O *1s* XPS peaks could be deconvoluted into three peaks (labelled as O_I, O_{II}, O_{III}). The peak at the binding energy of 529.61 eV corresponds to O_I, which is typical for lattice oxygen species (M-O bond). The peaks located at 531.36 eV, and 532.30 eV are ascribed to the under-coordinated oxygen in the lattice (O_{II}) and oxygen absorbed on the surface (O_{III}), respectively (**Figure 6.8a**) [48,49]. The high-resolution Co *2p* scan could be deconvoluted to the peaks corresponding Co^{2+} and Co^{3+} oxidation states, as shown in **Figure 6.8b**. The peak positioned around 782.29 and 797.95 eV corresponds to the binding energy of Co $2p_{3/2}$ and Co $2p_{1/2}$ of the Co^{2+}, while the peak observed at 780.24 eV and 796.14 eV are attributed to Co $2p_{3/2}$ and Co $2p_{1/2}$ of Co^{3+}, respectively [33,46,50]. The wide scan of Ni *2p* XPS spectra shown in **Figure 6.8c** depicts the spin-orbital characteristics of both Ni^{2+} and Ni^{3+}. The peak centred at 855.09 eV and 872.75 eV corresponds to $Ni^{2+,}$ while those at 856.34 eV and 875.07 eV are ascribed to Ni^{3+}. In addition to these peaks, a relatively weaker peak corresponding to metallic Ni (851.38 eV) is also observed, possibly due to oxygen vacancies. The peak located at around 933.84 eV, and 954.14 eV corresponds to Cu $2p_{3/2}$ and Cu $2p_{1/2}$ of the Cu^{2+}, whereas the peak at the binding energies of 932.65 eV and 952.47 eV are attributed to the Cu $2p_{2/3}$, Cu $2p_{1/2}$ from Cu^{1+} state (**Figure 6.8d**). Cu is present in both +2 and +1 oxidation states. The transition of Cu from +2 to the +1 valence state creates oxygen vacancies in the lattice [262].

Table 6.1 Comparison of photodegradation of methylene blue dye by different multicomponent oxides as catalysts.

Catalysts	Catalysts quantity (mg)	Time (min)	Degradation (%)	Source of light	Ref
CoO-ZnO	50	20	98	Sunlight	[244]
$ZnO/NiFe_2O_4$	75	70	95	UV light	[242]
$La_{1-x}Ca_xMnO3$	70	360	73	Visible light	[60]
10%Ca doped NiO	10	120	98.15	UV light	[257]
0.5 Wt.% Ca doped TiO_2	20	90	99.88	9 W LED bulb	[241]
$Gd_{0.2}La_{0.2}Ce_{0.2}Hf_{0.2}Zr_{0.2}O_2$	20	180	75	Sunlight	[170]
$Gd_{0.2}La_{0.2}Y_{0.2}Hf_{0.2}Zr_{0.2}O_2$	20	180	75	Sunlight	[170]
$(Ce_{0.2}Zr_{0.2}La_{0.2}Pr_{0.2}Y_{0.2})O_2$	40	20	98	300 W xenon lamp	[32]
(Co, Mg, Ni, Cu, Zn) O	25	180	18	300 W xenon lamp	[114]
(Mg,Co,Ni,Cu,Zn) O	**60**	**80**	**40**	**100 mW/cm2 solar simulator**	**Present study**
$(Mg,Co,Ni,Cu,Zn)_{0.9}Ca_{0.1}$ O	**60**	**80**	**98**	**100 mW/cm2 solar simulator**	**Present study**

A fraction of both Co and Ni is present in the higher valence state (+3)leading to the creation of metal vacancies. Thus, the large size of the Ca^{2+} ion in the lattice is accommodated by creating both oxygen and cation vacancies [264]. The Ca^{2+} *2p*

XPS peak of the synthesized sample is deconvoluted into three fitted peaks with characteristic spin-orbit splitting of Ca^{2+}.

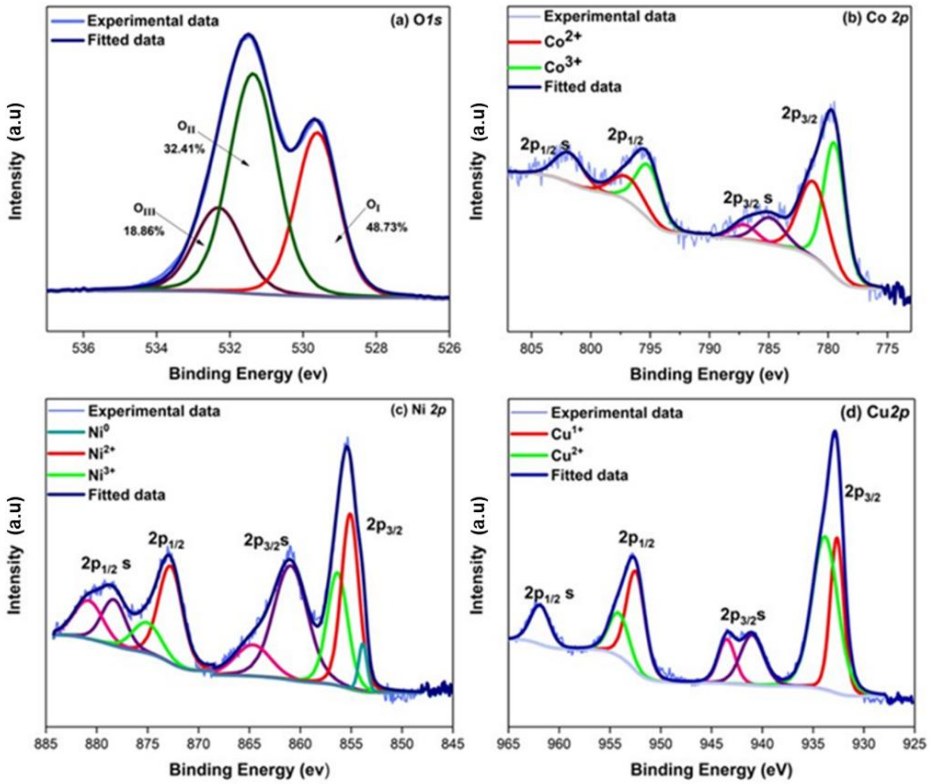

Figure 6.8 XPS spectra of nanocrystalline TM-HEO10 before the photocatalytic activity. (a) O1s (b) Co 2p (c) Ni 2p, and (d) Cu 2p XPS spectra, which highlights the change in valency of cation to accommodate large size Ca^{2+}.

In addition to $2p_{3/2}$ (347.01 eV) and $2p_{1/2}$ (350.57 eV), a peak located around (349.04 eV) is ascribed to the MgKLL auger peak, which confirms the presence of magnesium in the lattice (**Figure 6.9**). The wide scan of Zn *2p* could be deconvoluted into two peaks at the binding energies of $2p_{3/2}$ (1021.37 eV), and $2p_{1/2}$ (1044.46 eV). The difference between the binding energies of $2p_{1/2}$ and $2p_{3/2}$ (~23 eV) confirms the presence of Zn^{2+}. The XPS spectra for Zn^{2+} are nearly the same

for all samples. Further, it was noticed that the fraction of Ni and Co ions in the +3 state was greater in the Ca^{2+} incorporated sample (TM-HEO10). For instance, in the case of TM-HEO0, the fraction of Ni^{3+}/Ni^{2+} and Co^{3+}/Co^{2+} estimated from the XPS spectra (**Figure 6.10**) were 0.25 and 0.28, which increased to 0.31 and 0.46 respectively in TM-HEO10 (**Table 6.2**). The presence of a larger fraction of Cu^{1+} creates more oxygen vacancies in TM-HEO10, which was also confirmed by comparing the O *1s* spectra of both catalysts (TM-HEO10 and TM-HEO0).

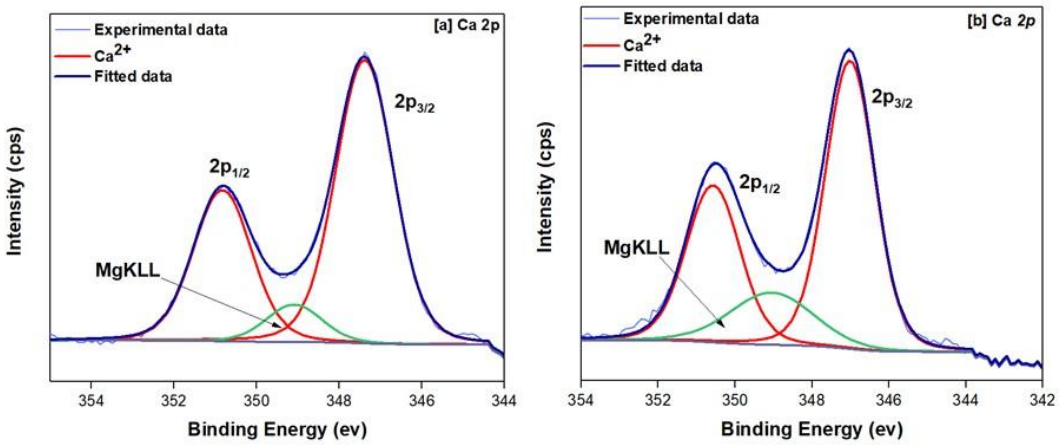

Figure 6.9 High resolution XPS spectra of Ca *2p* (a) before photocatalysis (b) after photocatalysis.

Thus, the incorporation of larger Ca^{2+} cations is compensated by Co, and Ni taking higher valence states (or creating metal vacancies) and creating oxygen vacancies. The increase in the fraction of Co and Ni in a higher oxidation state increases covalency. The covalency percentage (F_c) in TM-HEO0 and TM-HEO10 was estimated from the binding energy of O *1s* XPS spectrum [51]. It was observed that covalency in TM-HEO10 is 19.7%, which is significantly higher than that of 13.54% for TM-HEO0. Another reason for the increase in covalency can be

ascribed to the decrease in lattice oxygen in TM-HEO10, as seen from O *1s* XPS spectra. The increased covalency in TM-HEO10 oxide system results from greater hybridization between O *2p* and TM *3d* orbital, facilitating a decrease in charge transfer energy and reducing the band gap.

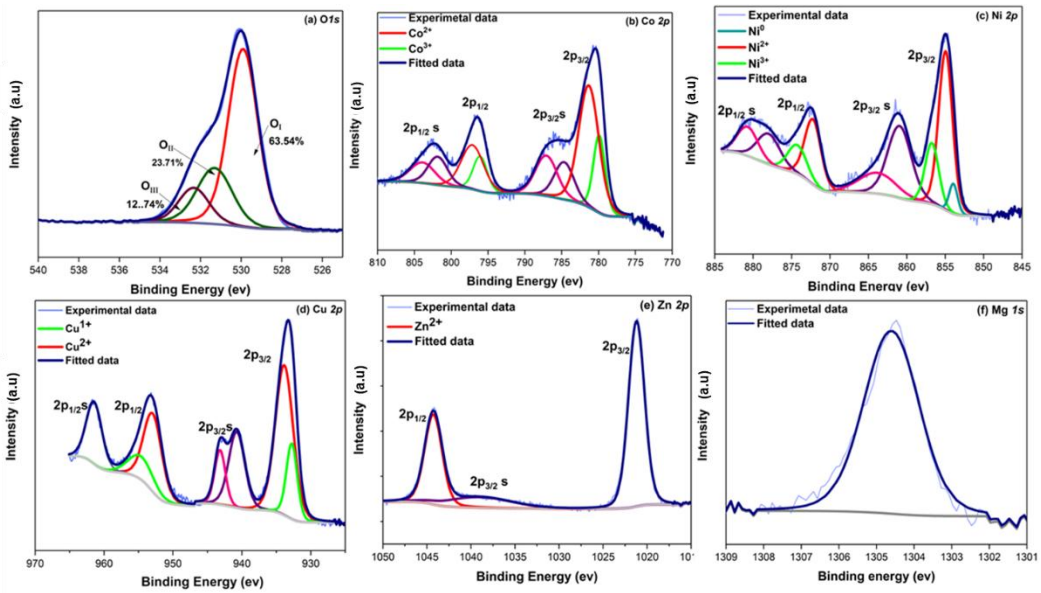

Figure 6.10 High resolution XPS spectra of (a) O1s (b) Co 2p (c) Ni2p (d) Cu 2p (e) Zn 2p for $(Mg,Co,Ni,Cu,,Zn)_{0.2}O$ HEO.

The reduction in band gap enhances the photocatalytic activity by utilizing a greater part of the solar spectrum; at the same time, vacancies also play an important role in improving the photocatalytic behaviour [40,59].

Table 6.2 Fraction of elements present in TM-HEO0, and TM-HEO10 (before and after photodegradation) in their respective oxidation state.

Element		TM-HEO0 (%)	N.C	TM-HEO10 (%) (Before Photocatalysis)	N.C.
Co	+2	6.32	12.64	4.97	9.94
	+3	2.35	7.05	3.64	10.92
Ni	0	0.21	0	0.25	0
	+2	5.81	11.62	5.02	10.04
	+3	2.11	6.33	2.54	7.62
Mg	+2	6.96	13.92	5.02	10.04
Cu	+1	1.44	1.44	2.26	2.26
	+2	6.06	12.12	4.14	8.28
Zn	+2	7.81	15.62	5.76	11.52
Ca	+2			3.36	6.72
O	-2	39.19	-78.38	36.86	-73.72
Total sum of charges			2.36		3.62
Metal vacancy		1.18			1.82

*NC: Normalized Charge

6.3.7 Photocatalysis mechanism

Figure 6.11 shows a schematic that illustrate the mechanism for the degradation of dye. Upon exposure to visible light in the presence of a catalyst, electrons (e^-) are excited from the valence band (VB) to the conduction band (CB), creating positive

holes (h^+) in the VB. These charge carriers drive a series of reactions that generate reactive species such as superoxide ions (O_2^-) and hydroxyl radicals (•OH). These generated radicals play a crucial role in facilitating the redox reactions responsible for the effective degradation of MB dye [261,265,266].

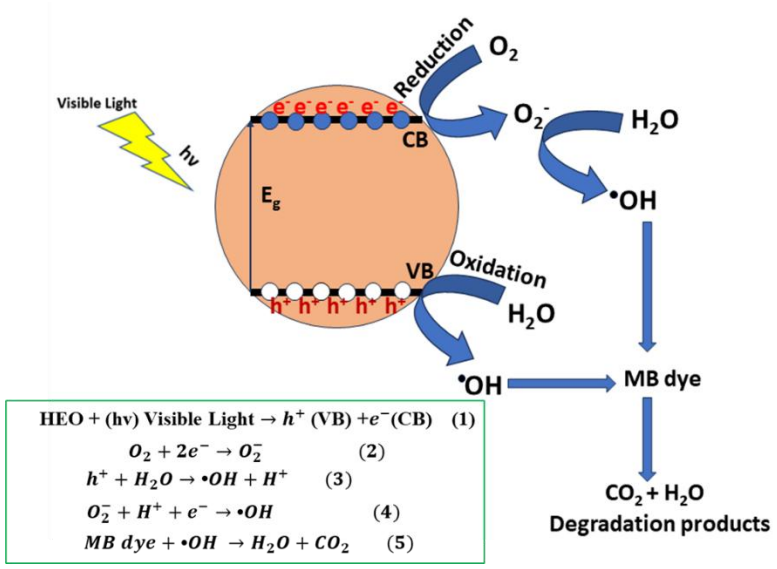

Figure 6.11 Schematic representation of a plausible mechanism of photodegradation of MB dye using HEOs as the catalyst using visible light as a source.

The metal cations, partially coordinated due to oxygen vacancies, exhibit a strong affinity for oxygen and water molecules, serving as active sites for the generation of •OH radicals. The substitution of Ca^{2+} into the TM-HEO0 lattice introduces defects, creates additional vacancies, and modifies the band structure. These changes, along with strong s-p and p-d exchange interactions, significantly enhance the photocatalytic performance of Ca^{2+} added samples (TM-HEO5 and TM-HEO10) [267].

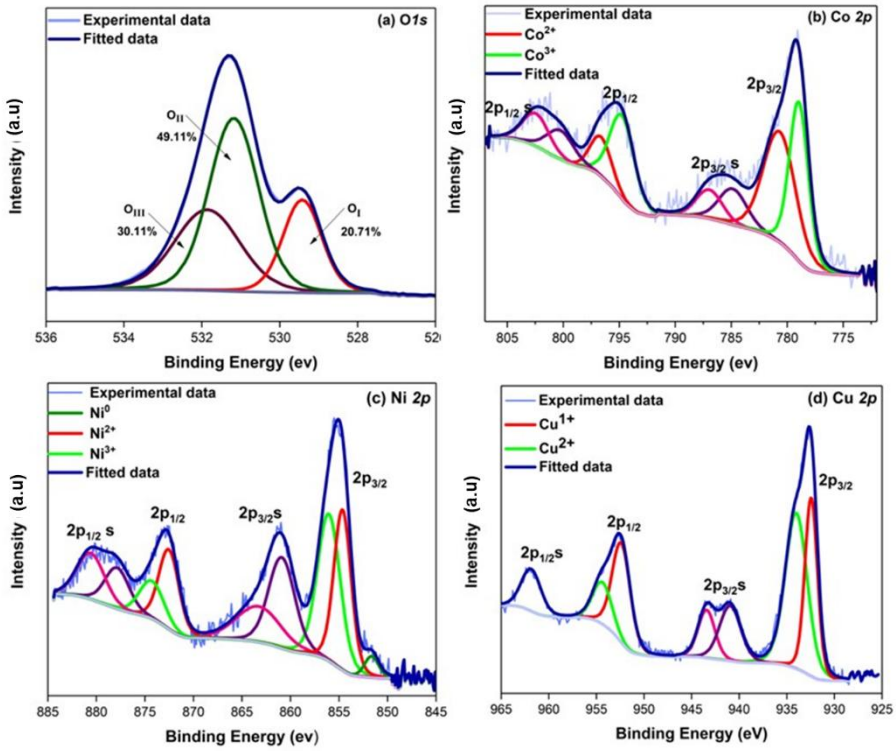

Figure 6.12 XPS spectra of nanocrystalline TM-HEO10 after the photocatalytic activity (a) O*1s* XPS spectra (b) Co *2p* XPS spectra (c) Ni *2p* XPS spectra (d) Cu *2p* XPS spectra.

The increased surface oxygen vacancies in the Ca^{2+} added catalysts act as electron scavengers, mitigating charge recombination and improving photocatalytic efficiency [248]. XPS analysis of the TM-HEO10 catalyst after MB dye degradation (**Figure 6.12**) reveals a higher surface-adsorbed oxygen content and a decreased O_I/O_{II} ratio, further confirming increased surface oxygen vacancies. Additionally, marginal increases in the Co^{3+}/Co^{2+} and Ni^{3+}/Ni^{2+} ratio (Table 6.2) suggest oxidation of Co^{2+} and Ni^{2+} during the degradation process, providing electron-donating sites that facilitate redox reactions (**Figure 8**). The valence band X-ray photoelectron spectra (VBXPS) of TM-HEO0 and TM-HEO10 catalysts,

both before and after photocatalysis, are depicted in **Figure 6.12(a)**. The valence band maxima (VBM) positions were determined using linear extrapolation of the band edge [268]. TM-HEO10 exhibits a higher VBM (1.13 eV) compared to TM-HEO0 (0.59 eV), indicating that the photoinduced holes possess sufficient positive potential to oxidize H_2O, effectively generating •OH radicals responsible for MB dye degradation. The apparent conduction band minima (CBM) were calculated using the band gap and VBM values.

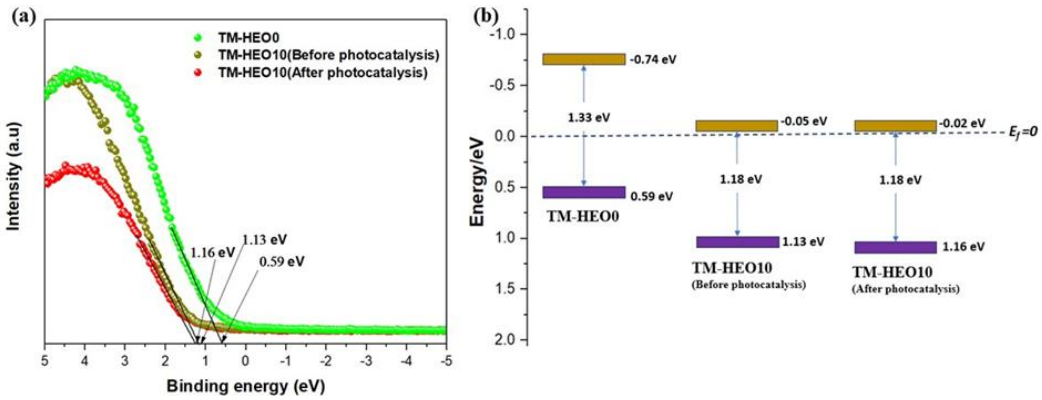

Figure 6.13 (a) VB-XPS of TM-HEO0(green) and TM-HEO10 before photocatalysis (brown), and TM-HEO10 after photodegradation (red) of methylene blue dye indicate shifting of the conduction band, (b) schematic of the band edges of VBM (purple) and CBM (golden) of TM-HEO0 and TM-HEO10 before and after photocatalysis.

TM-HEO10 demonstrated a band gap of 1.18 eV, with CBM positions of -0.05 eV before and -0.02 eV after photocatalysis (**Figure 6.12b**). Notably, the CBM shifted closer to the Fermi energy (E_f) post-photocatalysis, indicating an increase in free electron density. This shift highlights the role of oxygen vacancies in trapping

electrons, thereby minimizing charge recombination and enhancing the photocatalytic performance of the TM-HEO10 catalyst.

To sum up, on substituting calcium for transition metal ions in the five-component TM-HEO0, various factors contribute synergistically, which enhances the effectiveness of the photocatalytic dye degradation. The enhancement of the degradation efficiency can be broken down into two major components:

1. Greater absorption of solar spectrum: Co^{2+} and Ni^{2+} take higher valences (creating metal vacancies) to accommodate the large size of calcium ions Ca^{2+}, increasing the covalency of the system, which lowers the charge transfer energy (being the electron donating site). At the same time, some of the Cu^{2+} ions go into the +1 oxidation state to compensate for the charge and maintain the charge neutrality, creating oxygen vacancies, which act as electron scavengers and reduce the chances of charge recombination. Each constituent oxide in TM-HEO0 has distinct electronegativity (χ) and crystal field splitting (Δ). These differences introduce multiple 3d states in the five-component HEO within the native band gap, effectively making it narrow [45]. On the other hand, the fractions of Cu present in +1 valence state and lower the crystal field splitting (Δ). As a result, reducing the band gap. The introduction of a lower energy $Ca2^{+}$ 3s state than the TM 4s state in the conduction band also contributes towards further lowering of the band gap [45,47]. A lower bandgap enhances the absorption of a greater part of the solar spectrum.
2. Enhancement of degradation sites: The metal cations, which are not fully coordinated due to the presence of oxygen vacancies, have a greater affinity for oxygen and water molecules, acting as •OH radicals generating sites, where dye pollutants are preferentially adsorbed and degraded. At the same time, the increase in the specific surface area increases the number of sites per unit mass, thereby making the catalyst more effective.

6.4 Conclusions

We synthesized nanocrystalline $(Mg,Co,Ni,Cu,Zn)_{1-x}Ca_xO$ (x = 0,0.05, 0.1) high entropy oxide powders via solution combustion synthesis method and calcined at 1373 K. The XRD analysis revealed a single-phase rocksalt solid solution in both pristine and Ca^{2+} added samples. On Ca^{2+} doping, crystallite size decreases due to the strain in the lattice as larger ions are accommodated by inducing strain and defects in the lattice. Owing to the smaller crystallites, Ca^{2+} substituted samples show a larger surface area. Further, to accommodate the large isovalent cation (Ca^{2+}), a greater fraction of Co and Ni goes into the +3 oxidation state, which increases the covalency of the system, enabling a greater hybridization between '*p*' and '*d*' orbital, lowering the band gap. The oxidation of Co^{2+} and Ni^{2+} to the higher valency creates metal vacancies. To compensate for the higher oxidation state of Co and Ni, a fraction of Cu and Ni also goes into the lower oxidation states, causing the generation of additional oxygen vacancies in Ca^{2+} added samples. The increased oxygen vacancies on the surface Ca^{2+} doped catalyst acts as an electron scavenger, which inhibits the recombination of photoinduced electrons and holes. The photodegradation of MB dye enhanced about 6 times when a 10 at.% Ca^{2+} is incorporated into the five components (Mg,Co,Ni,Cu,Zn)O. This work gives insight into the possibility of exploring non-equimolar high entropy oxides for functional applications such as photocatalysis.